

Article

# Simulating Binary Neutron Stars with Hybrid Equation of States: Gravitational Waves, Electromagnetic Signatures, and Challenges for Numerical Relativity

Henrique Gieg<sup>1,\*</sup>, Tim Dietrich<sup>2</sup>, Maximiliano Ujevic<sup>1</sup>

<sup>1</sup> Centro de Ciências Naturais e Humanas, Universidade Federal do ABC, 09210-170, Santo André, São Paulo, Brazil

<sup>2</sup> Nikhef, Science Park, 1098 XG Amsterdam, The Netherlands

\* Correspondence: henrique@gieg.com.br

Version August 9, 2019 submitted to *Particles*

**Abstract:** The gravitational wave and electromagnetic signatures connected to the merger of two neutron stars allow us to test the nature of matter at supranuclear densities. Since the Equation of State governing the interior of neutron stars is only loosely constrained, there is even the possibility that strange quark matter exists inside the core of neutron stars. We investigate how strange quark matter cores affect the binary neutron star coalescence by performing numerical relativity simulations. Interestingly, the strong phase transition can cause a reduction of the convergence order of the numerical schemes to first order if the numerical resolution is not high enough. Therefore, an additional challenge is added in producing high-quality gravitational wave templates for Equation of States with a strong phase transition. Focusing on one particular configuration of an equal mass configuration consistent with GW170817, we compute and discuss the associated gravitational wave signal and some of the electromagnetic counterparts connected to the merger of the two stars. We find that existing waveform approximants employed for the analysis of GW170817 allow describing this kind of systems within the numerical uncertainties, which, however, are several times larger than for pure hadronic Equation of States, which means that even higher resolutions have been employed for an accurate gravitational wave model comparison. We also show that for the chosen Equation of State, quasi-universal relations describing the gravitational wave emission after the moment of merger seem to hold and that the electromagnetic signatures connected to our chosen setup would not be bright enough to explain the kilonova associated to GW170817.

**Keywords:** Numerical Relativity, Equation of State, Binary Neutron Stars, Gravitational Waves, Phase Transition, Strange Quark Matter

---

## 1. Introduction

The observation of gravitational waves (GWs), GW170817, and electromagnetic (EM) signatures, AT2017gfo and GRB170817A, originating from the same astrophysical source have initiated a new era of multi-messenger astronomy [1–3].

Because of their large compactness, neutron stars (NSs) contain matter at supranuclear densities, which makes them a perfect laboratory to determine matter under extreme conditions governing the NS interior. Today's Equation of State (EoS) constraints inferred from GW170817 arise from the analysis of the GW signal, e.g., [1,4–8] or from a combined GW and EM analysis, e.g., [9–13]. In addition, one can also

perform statistical analyses of a large set of possible EoSs incorporating information from nuclear physics theory, e.g., [14,15].

The current analysis of GW170817 disfavors NSs with too large radii and tidal deformabilities, the exact state of the supranuclear matter inside the NS core is still unknown. While recent first-principle studies disfavor the presence of strange quark matter (SQM) inside NSs with masses  $\lesssim 1.4M_{\odot}$ , Ref. [16], it is not clear if more massive NSs could have SQM cores or if the merger could undergo a strong phase transition [17,18].

In this article, we study possible effects of SQM during the binary coalescence, for this purpose, we solve the equations of general relativity combined with the equations of general relativistic hydrodynamics (GRHD) with the help of full 3+1 -dimensional (3 dimensions in space and 1 dimension in time) numerical relativity (NR) simulations. Such simulations allow a characterization of the GW and EM radiation. Over the last years, the NR community has made significant progress in simulating neutron star spacetimes on many fronts, e.g., extending the simulation's accuracy, incorporating microphysical models in the simulations, and exploring different regions of the binary neutron star (BNS) parameter space [19–27,27–33]. We will show that standard techniques are capable of dealing with NSs containing hadronic and SQM. Up to our knowledge, most previous simulations with EoSs allowing strong phase transitions have studied the imprint of a SQM phase after the merger of the two stars [17,18], in addition, also the phenomenological implications of the two-families scenario (in which hadronic stars and pure strange quark stars coexist) has been recently analysed [34], but no numerical relativity inspiral simulation with stars containing SQM has been performed. Thus, the effect of employing a hybrid EoS, in which hadrons convert into strange quarks through a thermodynamical phase transition, on the inspiral, has to be investigated in more detail. We find that a strong phase transition impairs the NR inspiral evolution and that the convergence order of the simulations can drop to first order if the employed resolutions are not sufficient. While it might be possible to deal with phase transitions incorporating more sophisticated numerical techniques or higher resolutions, our work is (up to our knowledge) the first to point out this arising complication.

The structure of the article is as follows. First, we discuss how we construct a hybrid star EoS using the tdBag model, we continue by describing the employed setup and numerical techniques. Then, we present a first qualitative description of the binary coalescence and continue by discussing the GW emission during the inspiral and postmerger phase, as well as, the related ejecta outflow and expected EM counterparts. Unless otherwise stated, we employ geometric units, i.e.,  $G = c = 1$ . Physical units are sometimes given for better intuition.

## 2. A new hybrid Star Equation of State

### 2.1. tdBag model for strange quark matter

tdBag [35] is a bag-like model inspired by the standard MIT bag model [36,37]<sup>1</sup>. It incorporates features expected for cold strange quark matter composed of up, down, and strange quarks in free Fermi seas resulting from the deconfinement, i.e., the breaking of hadronic matter into its constituents once baryon densities compatible to the nuclear density  $n_0 \sim 0.16 \text{ fm}^{-3}$  are reached. tdBag accounts for perturbative effects of strong interaction between quarks [38] and the effects of color superconductivity at low temperatures [39]. There are many possible color superconducting phases, in this work we assume that quarks are in the color-flavor-locked phase (CFL) [39,40], in which the three quark flavors are symmetric (equal baryon density of up, down and strange) and exhibit superfluidity.

---

<sup>1</sup> For convenience we will use natural units in this section setting  $\hbar = c = 1$ .

In the massless up and down quarks approximation  $m_u = m_d = 0$ , the tdbag model is defined by the grand potential per volume ( $\Omega$ ) as

$$\Omega = -\frac{3}{4\pi^2}a_4\mu^4 + \frac{3}{4\pi^2}a_2\mu^2 + B + \Omega_e, \quad (1)$$

where  $a_4$ ,  $a_2$ , and  $B$  are free parameters and  $\mu \equiv (\mu_u + \mu_d + \mu_s)/3$  is the quark chemical potential,  $\mu_i$  refers to the chemical potential of the  $i$ -th flavor, and  $\Omega_e$  is the electrons' contribution. Before proceeding to the construction of hybrid EoS containing a SQM core, we are going to briefly discuss the meaning of the parameters presented in Eq. (1):

1. The quartic coefficient  $a_4$  can be interpreted as a correction to the pressure of the free Fermi sea arising from quantum chromodynamics (QCD). Fraga et al. [41] show that, to second order in the strong coupling constant, a reasonable value for this parameter is  $a_4 \sim 0.7$ . The values of  $a_4 = 0$  and  $a_4 = 1$  correspond to maximum or none QCD interaction, respectively.

2. The quadratic coefficient  $a_2$  accounts for the contribution of the strange quark mass and color superconductivity. The value of this parameter is given by  $a_2 = m_s^2 - 4\Delta^2$ , where  $m_s \sim 100$  MeV is the strange quark mass and  $\Delta \sim 0 - 100$  MeV is the energy gap between free and Cooper pairs of quarks [38,40,42].

3. The bag constant  $B$ , introduced phenomenologically into the theory to describe the deconfinement, is the energy density required to produce a "vacuumless" volume in which quarks exist.

4. The contribution of the electron potential ( $\Omega_e$ ) for our purposes is negligible; cf. Ref. [43] and references therein. Nevertheless, if the SQM is not in the CFL phase [40] there must be electrons within the quark phase to ensure (i) local charge neutrality and (ii) chemical equilibrium. These two conditions may be expressed respectively as

$$\frac{2}{3}n_u - \frac{1}{3}n_d - \frac{1}{3}n_s = n_e, \quad (2)$$

$$\mu_d = \mu_s = \mu_u + \mu_e, \quad (3)$$

where  $n_i$  denotes the number density. For SQM in the CFL phase, the quark matter is symmetric, thus, local charge neutrality is satisfied without the presence of electrons. In both cases, CFL ( $\Omega_e = 0$ ) or non-CFL phase (neglecting  $\Omega_e$ ), Eq. (1) leads to an analytical EoS for SQM.

## 2.2. Thermodynamics and parameter analysis

In this section we constrain the parameter space ( $a_4, a_2, B$ ) presented in Eq. (1) assuming the absolutely stable strange quark matter hypothesis [44,45] and thermodynamic properties. With the help of the grand potential  $\Omega$ , we found that the pressure  $p$ , the baryon number density  $n_b$ , and the energy density  $\epsilon$  can be written as

$$p = -\Omega = \frac{3}{4\pi^2}a_4\mu^4 - \frac{3}{4\pi^2}a_2\mu^2 - B, \quad (4)$$

$$n_b = -\frac{1}{3}\frac{\partial\Omega}{\partial\mu} = \frac{1}{2\pi^2}(2a_4\mu^3 - a_2\mu), \quad (5)$$

$$\epsilon = -p + 3\mu n_b = \frac{9}{4\pi^2}a_4\mu^4 - \frac{3}{4\pi^2}a_2\mu^2 + B. \quad (6)$$

It is possible to obtain  $p(\epsilon)$  from Eq. (4), (5) and (6), and the result is

$$p(\epsilon) = \frac{1}{3}(\epsilon - 4B) - \frac{a_2^2}{12\pi^2 a_4} \left( 1 + \sqrt{1 + \frac{16\pi^2 a_4}{a_2^2} (\epsilon - B)} \right), \quad (7)$$

which is the analytical EoS for SQM parametrized by  $a_4$ ,  $a_2$ , and  $B$ .

As long as we are dealing with a phenomenological model, it is of fundamental importance to constrain the parameter space within a region in which it can produce EoSs for stellar matter. To justify our next choices, we make a digression on the absolutely stable strange quark matter hypothesis (i.e. no strange matter will decay into hadronic matter under a thermodynamic process), proposed by Bodmer [44] and Witten [45]. They consider the ground state of matter to be three Fermi seas of deconfined quarks in equal proportions of up, down and strange flavors. The reason for this is that the energy per baryon ( $E/A$ ) in the ground state is smaller than that of the most stable pressureless nuclei,  $^{56}\text{Fe}$  with  $E/A \sim 930$  MeV. Until now, no experimental observations could refute this hypothesis. Indeed, as deconfinement is expected to take place under extreme conditions such as the ones in the core of compact stars, many efforts have been made to uncover which observables in astrophysical phenomena could rule out or confirm the existence of SQM in stars.

In the case of a Hybrid Star (HyS), i.e., a star containing a SQM core surrounded by hadronic matter (HM), the deconfinement of HM into SQM must take place at a strictly positive pressure. Assuming that the deconfinement is a first order phase transition, i.e., the interface between the hadron and quark phases is characterized by a sharp discontinuity (no mixed phase is present). At the interface the Gibbs condition must be satisfied

$$g_q(p) = g_h(p), \quad (8)$$

where  $g_q$ ,  $g_h$  are the Gibbs free energy per baryon of the quarks and hadrons, respectively, with the generic  $g$  given by

$$g = \frac{\epsilon + p}{n_b} = 3\mu. \quad (9)$$

Eq. (8) represents chemical and mechanical equilibrium at the interface. Using Eqs. (9) and (4), one can write  $p$  as a function of the Gibbs free energy

$$p(g) = \frac{a_4}{108\pi^2} g^4 - \frac{9a_2}{108\pi^2} g^2 - B. \quad (10)$$

To enforce the phase transition pressure to be strictly positive ( $p > 0$ ), the following relation must hold

$$B > \frac{g^2}{108\pi^2} (a_4 g^2 - 9a_2). \quad (11)$$

According to the absolutely stable SQM hypothesis the minimum of  $g$  is  $g_{\min}(p = 0) \approx 930$  MeV. This value of  $g$  sets  $B_{\min}$ , for which hadronic matter deconfines in three quark flavors, such that

$$B_{\min} = \frac{g_{\min}^2}{108\pi^2} (a_4 g_{\min}^2 - 9a_2). \quad (12)$$

This equation defines the region on the  $B$ ,  $a_2$ ,  $a_4$  space above which a transition from HM to SQM happens. On the other hand, the hadronic part of the HyS must not be in metastable equilibrium, i.e., one shall guarantee that it would not decay in 2-flavor quark matter. This condition can be ensured if

$$g_{2f} > g_h, \quad (13)$$

where  $g_{2f}$  is the Gibbs free energy per baryon for 2-flavor quark matter. A second similar condition for  $B$  can be found [43] adapting Eq. (1) to the  $2f$  case in the massless approximation ( $m_u = m_d = 0$ ), the result is

$$B > \bar{B}_{\min},$$

$$\bar{B}_{\min} = \frac{\delta_{\min}^2}{54\pi^2} \left[ \frac{4\delta_{\min}^2 a_4}{(1 + 2^{1/3})^3} - 3a_2 \right]. \quad (14)$$

Therefore, conditions (12) and (14) constrain the parameters space  $(a_4, a_2, B)$  in three regions (see Fig. 1 for an example),

- (i)  $B < \bar{B}_{\min}$ : not allowed region due to the fact that hadronic matter is more stable than quark matter, then we cannot use a SQM EoS.
- (ii)  $\bar{B}_{\min} < B < B_{\min}$ : absolutely stable strange stars (SS). There is no phase transition  $\text{HM} \rightarrow \text{SQM}$  and the star is entirely made of 3-flavor quarks.
- (iii)  $B > B_{\min}$ : HyS. There exists a phase transition between HM and SQM for some energy density  $\epsilon$ .

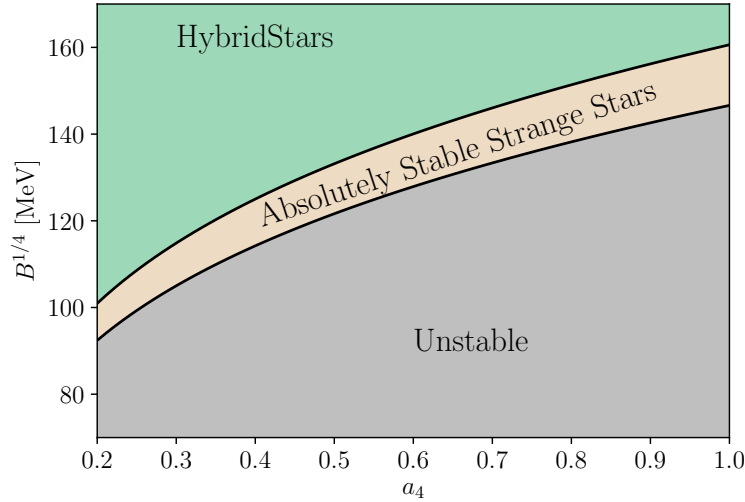


**Figure 1.** Parameter space  $(a_4, B)$  for fixed  $a_2 = 5000 \text{ MeV}^2$ . We identify three different regions. The upper region where  $\text{HM} \rightarrow \text{SQM}$  transitions are possible and describes a HyS. The middle region where SQM is absolutely stable and we found strange stars. The lower region is prohibited due to the instability of SQM.

The EoS for SS is given directly by Eq. (7). To obtain the EoS for HyS we must solve Gibbs condition (8) with the help of a hadronic EoS to find the deconfinement pressure  $p_T$  and the corresponding energy densities  $\epsilon_h$  and  $\epsilon_q$  for hadronic and quark matter, respectively. Assuming a first order phase transition, the HyS EoS is then constructed as a piecewise function with the prescription

- (i)  $\epsilon \leq \epsilon_h$ : HM EoS,
- (ii)  $\epsilon_h < \epsilon < \epsilon_q$ :  $p = p_T$ ,
- (iii)  $\epsilon \geq \epsilon_q$ : SQM EoS.

If deconfinement produces a sharp discontinuity between the phases or an extended region in which hadrons and quarks are mixed, is an open question that relies primarily on how global electric charge neutrality is achieved by the star. This could happen in two scenarios: (i) assuming local charge neutrality, i.e., that the electric charge density is zero everywhere in the stellar interior or (ii) assuming that electric charge density is non-zero and distributed within the star such that the total charge is zero. Despite the

latter being a relaxation of the first condition, it has profound implications for the star's structure, e.g. the rise of Coulomb interactions between quarks in different geometrical shapes (drops, rods, and slabs) and the surrounding hadronic matter may lead to a mixed phase of quarks and hadrons extending along the stellar interior [46]. On the other hand, if local charge neutrality is considered, quarks and hadrons separate into two phases with a sharp discontinuity interface between them. The existence of a mixed phase is favored if the Coulomb interactions were to lower the system's energy [46] in comparison to maintain the interface by surface tension. Recently, it had been shown [47] that it is energetically favorable for SQM to sharp discontinuity interface if the quark matter is described by the Nambu-Jona-Lasinio model [48].

### 2.3. Building hybrid star EoS

The recent observation of GWs from GW170817 established constraints on the NS EoS. The analysis of the data favored soft EoS instead of stiff EoS. For our analysis, we use for the HM phase the SLy EoS [49], which is currently in agreement with EoS constraints. Recalling that we assumed the deconfinement as a first order phase transition (at the sharp interface between quarks and hadrons) the Gibbs conditions (8) must hold for both phases.

We start writing  $g$  as a function of  $p$  for both phases. This is straightforward for the SQM, solving Eq. (10) for  $g$ , one obtains

$$g_q(p) = \left\{ \frac{9a_2}{2a_4} \left[ 1 + \sqrt{1 + \frac{(4\pi)^2 a_4}{3a_2^2} (p + B)} \right] \right\}^{1/2}. \quad (15)$$

For the chosen hadronic EoS, we construct the Gibbs free energy per baryon with the definition

$$g = \frac{\epsilon + p}{n_b},$$

from which we obtain an expression for  $g_h \equiv g_h(p)$  by interpolating the hadronic EoS. The Gibbs condition (8) can be satisfied numerically by finding the root of  $f(p) = g_q(p) - g_h(p)$ . The result is the pressure  $p_T$  at which the two curves  $g(p)$  meet (see Fig. 2) and corresponds to the constant pressure along the phase transition. The value  $g_T = g(p_T)$  is the common Gibbs free energy per baryon. The next step is to obtain the energy density  $\epsilon$  associated with  $p_T$  (or  $g_T$ ) for both EoS. In the case of SQM, from Eqs. (6) and (9), we obtain

$$\epsilon_q = \frac{a_4}{36\pi^2} g_T^4 - \frac{a_2}{12\pi^2} g_T^2 + B, \quad (16)$$

which sets the energy density at the phase transition for the SQM phase. Similar calculations in the hadronic phase must be carried out to find  $\epsilon_h$ . The final result is a HyS EoS produced by connecting the hadronic EoS to the SQM EoS Eq. (7) with  $p = p_T$  for  $\epsilon_h < \epsilon < \epsilon_q$ , as shown in Fig. 2.

### 2.4. HyS EoS as piecewise polytropes

For the dynamical evolution of the binary HyS with the BAM code [50–53] and to calculate the initial condition using the SGRID code [54], we express the EoS as a piecewise polytrope (PwP):

$$p(\rho) = K_i \rho^{\Gamma_i}, \quad d\left(\frac{\epsilon}{\rho}\right) = -pd\left(\frac{1}{\rho}\right), \quad \rho_{i-1} < \rho < \rho_i \quad (17)$$

with  $K_i$  and  $\Gamma_i$  being defined in the individual intervals  $\rho_0 < \dots < \rho_i < \dots < \rho_n$  such that the continuity of  $p(\rho)$  is guaranteed.

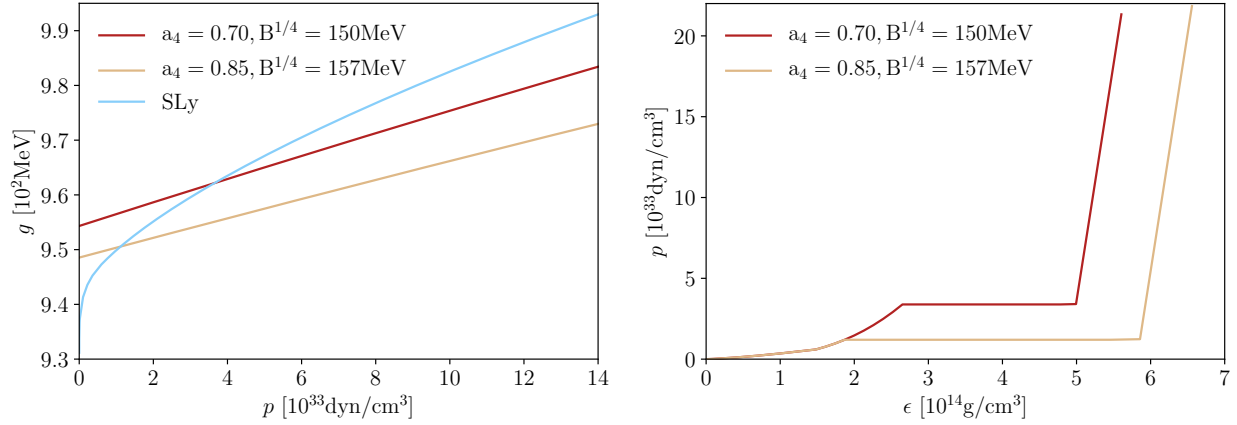


**Figure 2.** Left panel: Gibbs free energy  $g$  as function of pressure  $p$ . For the SQM EoS we set  $a_2 = 5000$   $\text{MeV}^2$ . The point at which SLy and SQM curves intersect determines the transition pressure  $p_T$  and the transition Gibbs free energy  $g_T$ . For pressures greater than  $p_T$  the SQM free energy becomes lower than the SLy free energy, thus being energetically favorable. Right panel: EoS for the HyS constructed by the junction of the SLy EoS and two parameter set for the SQM EoS. We assume a first order phase transition between hadronic and strange quark matter and we set  $a_2 = 5000$   $\text{MeV}^2$ .

The SLy part of our hybrid EoS uses the piecewise polytrope representation given in Ref. [55]. For the SQM phase, Eq. (7) has to be interpolated as polytropes in rest mass density. This is done producing a tabulated version of the SQM EoS and dividing this part of the EoS into fifteen pieces from which we built the SQM piecewise polytrope. The complete HyS piecewise polytrope can be found in Appendix A. In Fig. 3 we compare the results of the mass-radius curve for an isolated TOV star obtained using the tabulated EoS and the piecewise polytrope EoS. For the gravitational mass used in this article, we find a difference less than 0.5% in the star radius.

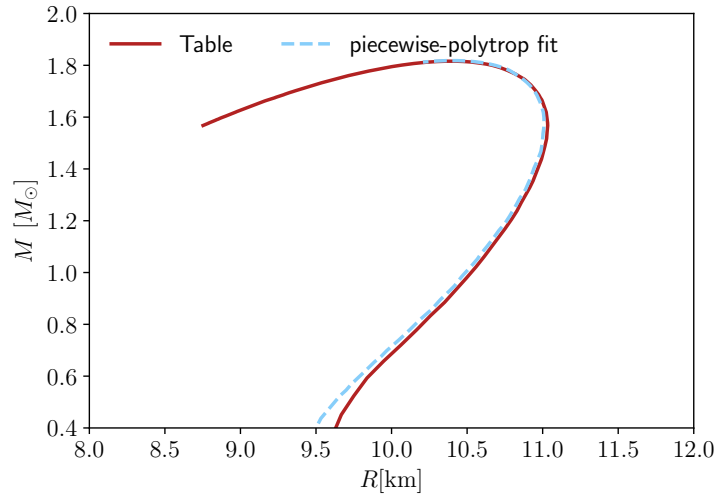


**Figure 3.** Mass-radius curves of the tabulated and piecewise-polytrope EoSs with  $a_4 = 0.70$ ,  $a_2 = 5000$   $\text{MeV}^2$  and  $B^{1/4} = 150$   $\text{MeV}$ .

### 3. Configurations details and numerical methods

#### 3.1. Hybrid star configuration

For our primary study of the binary HyS coalescence, we chose a setup which is close to the estimated binary properties of GW170817 (details are given in Tab. 1). Our configuration consists of two non-spinning stars with individual masses of  $M = 1.365M_{\odot}$ . The total mass of  $M = M^A + M^B = 2.73M_{\odot}$  is consistent with the estimated total mass of GW170817 ( $2.73^{+0.04}_{-0.01}M_{\odot}$ , Ref. [6]). The tidal deformability of the individual stars is  $\Lambda^{A,B} = 378.4$  and the radii of the stars are  $\sim 11.0\text{km}$ , which also agrees with current multi-messenger constraints arising from the analysis of the GW, the kilonova, and the short GRB [13] of  $R \in [10.9, 13.6]\text{km}$ .

**Table 1.** Properties of the employed configuration. The columns refer to the individual masses in isolation, the baryonic mass of the individual stars, the stars' compactnesses, the radii of the stars, the tidal deformability of the individual stars  $\Lambda^{A,B}$ , the ADM-mass and angular momentum of the system, and the estimated residual eccentricity  $e$ .

| $M^{A,B}[M_{\odot}]$ | $M_b^{A,B}[M_{\odot}]$ | $C^{A,B}$ | $R^{A,B}[\text{km}]$ | $\Lambda^{A,B}$ | $M_{\text{ADM}}[M_{\odot}]$ | $J_{\text{ADM}}[M_{\odot}^2]$ | $e$                |
|----------------------|------------------------|-----------|----------------------|-----------------|-----------------------------|-------------------------------|--------------------|
| 1.365                | 1.527                  | 0.18      | 11.0                 | 378             | 2.705                       | 8.324                         | $5 \times 10^{-3}$ |

#### 3.2. Numerical methods

We compute the initial configuration solving the conformal thin-sandwich equations [56–58] with the SGRID code [54,59,60]. SGRID uses pseudospectral methods to accurately compute spatial derivatives. We performed an iterative procedure to reduce the orbital eccentricity varying the system's initial radial velocity and eccentricity parameter, as discussed in [60–62], until eccentricity is  $\sim 10^{-3}$ .

Dynamical evolutions are performed with the BAM code [50–53], which uses the method of lines employing finite differences for the spatial discretization of the metric variables and a high-resolution shock-capturing (HRSC) scheme for the computation of the matter fluxes of the general relativistic hydrodynamics equations. The spacetime is evolved with the Z4c evolution system [63–65]. The BAM code employs an adaptive mesh refinement strategy with a hierarchy of nested Cartesian grids. The grid spacing of each level is half the grid spacing of its coarser parent level. A number of inner levels can be moved dynamically to cover the NS's during the evolution. In this article, we use 7 refinement levels labeled  $l = 0, \dots, 6$  from the coarsest to the finest. The detailed grid specifications for the employed resolutions are given in Tab. 2. The GRHD numerical fluxes are computed with a local Lax-Friedrich's (LLF) scheme and the fluid's characteristic variables are reconstructed using a fifth order weighted essentially non-oscillatory (WENOZ) algorithm [53,66]. The same GRHD settings have been employed in [21,53,67] leading to a 2nd order convergence of the GW phase independent of the configuration details.

**Table 2.** Grid configurations employed in the simulations for the different resolutions. The columns refer to the simulation's name, the number of moving boxes  $L^{\text{mv}}$ , the number of grid points per direction in the static levels  $n$ , the number of grid points per direction in the moving levels  $n^{\text{mv}}$ , the grid spacing in the innermost level  $h_6$  (corresponding to  $l = 6$ ), and the grid spacing of the coarsest level  $h_0$ .

| Name | $L^{\text{mv}}$ | $n$ | $n^{\text{mv}}$ | $h_6$ | $h_0$ |
|------|-----------------|-----|-----------------|-------|-------|
| R1   | 4               | 192 | 64              | 0.240 | 15.36 |
| R2   | 4               | 288 | 96              | 0.160 | 10.24 |
| R3   | 4               | 384 | 128             | 0.120 | 7.68  |
| R4   | 4               | 480 | 160             | 0.096 | 6.14  |



## 4. Quantitative Merger Dynamics

We start discussing our binary HyS mergers with a qualitative description of the coalescence of the two stars as depicted in Fig. 4. The first panel shows the initial setup for our evolution as computed from SGRID. The two stars have an initial coordinate separation of  $\sim 61.5\text{km}$ , which corresponds to a proper distance of  $\sim 76.4\text{km}$ . As visible in the figure, we use a gray scale for the SQM, while HM is shown on a blue to red scale. The second panel shows the system after approximately 6 orbits, i.e., 12 GW cycles. At this time one sees that the star's surface gets 'smeared out' and is not perfectly preserved. Thus, lower density material surrounds the two stars. Similar observations are typical for full NR simulations and have been discussed in e.g. [68] and references therein. The main reason for this, is the sharp transition of the density and the usage of an artificial atmosphere for the GRHD simulation, see e.g. [53]. A similar observation is true about three to four orbit before the moment of merger (third panel). The fourth panel shows the system at the merger, i.e., when the GW amplitude peaks. One sees that the two SQM cores of the individual stars come into contact at this time. After the moment of merger, the central density inside the SQM core increases. The formed remnant (fifth panel of Fig. 4) survives for about  $\sim 5$  milliseconds and undergoes two oscillations (three oscillations for lower resolutions) before it collapses to a black hole (BH). The final system (sixth panel) consists of a BH surrounded by an accretion disk composed of HM.

## 5. Gravitational Wave Signal

### 5.1. The Inspiral

We present the full gravitational waveform obtained from our simulations in Fig. 5 (top panel). Quantities related to the GW signal are plotted against the retarded coordinate time  $u$ , defined as

$$u = t - r_{\text{ext}} - 2M \ln(r_{\text{ext}}/2M - 1), \quad (18)$$

where we choose  $r_{\text{ext}} = 1000M_{\odot}$ . The inspiral is characterized by an increasing frequency and amplitude of the GW, the so-called chirp-signal. We find that the merger time (marked by a vertical line) shifts by several milliseconds between the different resolutions. It is important to point out that for similar resolutions, cf. [70,71], the dephasing and consequently the shift in the merger time between similar resolutions have been significantly smaller for EoSs without phase transition. The bottom panel of Fig. 5 shows the phase differences between individual resolutions. One finds that for the three lowest resolutions, the phase is only converging with first order with respect to the grid spacing. Rescaling the phase differences assuming first order convergence leads to very good agreement with the phase difference of lower resolutions (dashed yellow line). This is of particular importance since it has been pointed out that the combination of the high-order flux reconstruction for the characteristic variables with the 5th order WENOZ scheme leads to a clear second-order convergence of the GW phase [21,53,67] for a variety of hadronic EoSs employing the same resolution and code settings. Increasing the resolution, we find that second-order convergence is recovered (dash-dotted green line). Ref. [53] pointed out that the NS's surface causes this second-order convergence even though the numerical scheme is 5th order convergent for smooth hydrodynamical problems. Here, we find that in the case of a first order phase transition inside the NSs, the convergence order can even drop further to first order, but that with higher resolutions the convergence order increases. The reduced convergence order explains the large dephasing between the individual resolutions and displays the additional challenges in NR simulations of NS binaries employing a hybrid EoS.

Further work employing different hybrid EoSs and numerical schemes (varying the numerical flux scheme and limiters) is needed to understand if the observed feature is universal or might be caused by a

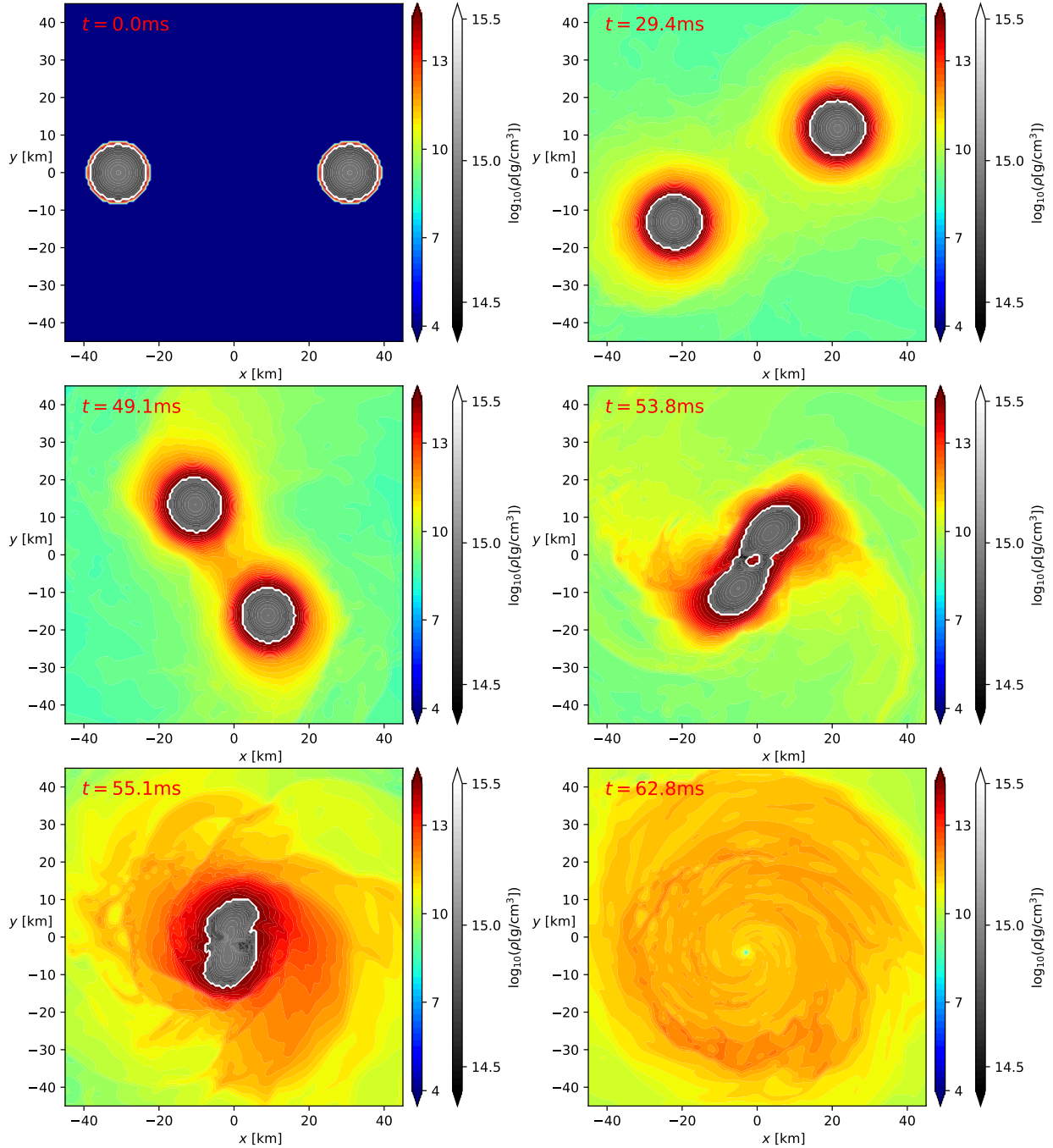


**Figure 4.** Density evolution within the orbital plane for different time snapshots for the R4 setup. We show the HM on a color scale ranging from blue to red and the SQM on a gray scale.

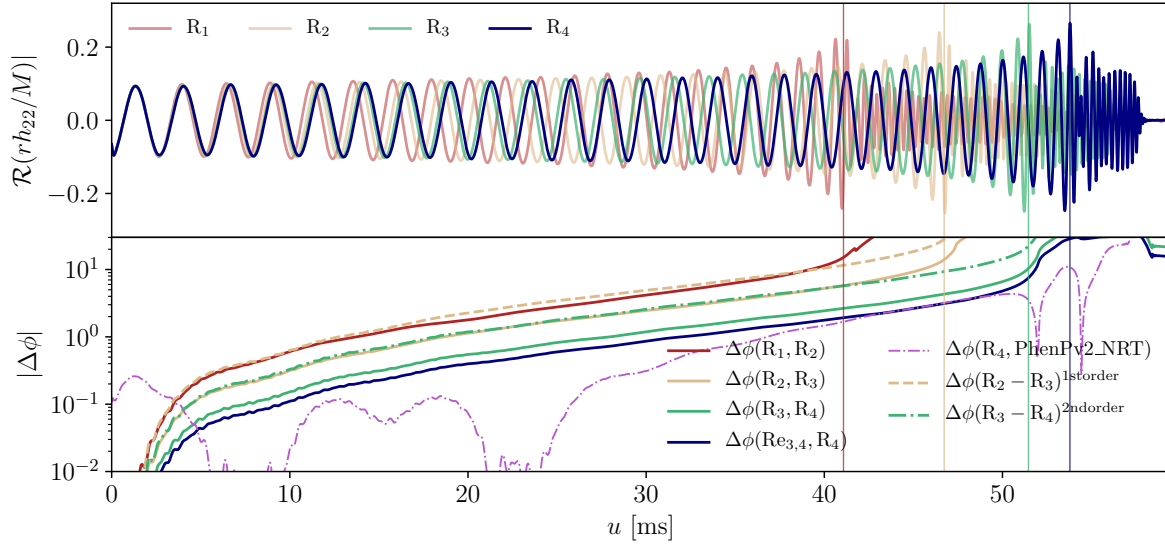


**Figure 5.** The top panel shows the (2,2)-mode of the GW signal for the different resolutions. The bottom panel shows the phase difference between the individual resolutions, where dashed lines show the phase difference rescaled to an assumed first or second order convergence. In addition, we show the phase difference with respect to a Richardson extrapolated waveform using resolutions  $R_3$  and  $R_4$ , denoted by  $Re_{3,4}$ . We also include the phase difference of  $Re_{3,4}$  with respect to the waveform approximant IMRPhenomPv2\_NRTidal [69] (purple dash-dotted line), denoted as PhenPv2\_NRT. Vertical lines mark the moments of merger for the individual resolutions.

particular choice of our parameters.

Finally, assuming second order convergence, we perform a Richardson extrapolation to obtain a better prediction for the GW phase, denoted by  $Re_{3,4}$ . We compare  $Re_{3,4}$  with the GW approximant IMRPhenomPv2\_NRTidal [21,69,72], which has been employed by the Ligo and Virgo Collaborations for the analysis of GW170817 in [6–8,73]. This approximant (IMRPhenomPv2\_NRTidal) is a phenomenological waveform model which has been developed for the description of BNS systems. During its construction only NR simulations with hadronic EOSs were used [21]. Therefore, we use this model to compare our results of hybrid star binaries with predictions for purely hadronic EOSs. The exact waveform IMRPhenomPv2\_NRTidal, which we compare to, uses the same masses and tidal deformabilities as our NR simulation. Finally, the IMRPhenomPv2\_NRTidal and our hybrid star waveform are aligned within a time window  $u \in [5, 10]$ ms by minimizing the phase difference within this interval to allow a reasonable comparison and to compute the phase difference. The phase difference between resolution  $Re_{3,4}$  and IMRPhenomPv2\_NRTidal is shown as a dash-dotted purple line in Fig. 5 (bottom panel). We find that until the moment of merger, the phase difference  $\phi(Re_{3,4}) - \phi(\text{IMRPhenomPv2\_NRTidal})$  is below the estimated error  $\Delta\phi(Re_{3,4}, R_4)$ <sup>2</sup>, which is the first validation of a waveform model against a NR dataset including a strong phase transition inside the star. That the difference between the NR data and the waveform approximant is below the uncertainty of the data strengthens the reliability of models used for GW data analysis even if these have been derived for purely hadronic EOSs. However, due to the reduced

<sup>2</sup> Note that the larger dephasing at the beginning of the simulation can be explained by junk radiation.

convergence order and the large phase error of our simulations, further evolutions with higher resolutions are required for a more quantitative and stronger test.

### 5.2. The Postmerger

After the merger of the two stars, the rotating merger remnant emits GWs due to its asymmetric shape (see the fifth panel of Fig. 4). The typical emission during the postmerger happens on frequencies ranging from 2 – 4kHz. Which frequencies are excited and the strength of each individual frequency depends on the properties of the merger remnant and, thus, on the mass, spin, and EoS of the binary. We refer to existing studies available in the literature, e.g., [52,70,71,74–83], for further details and discussions about the mechanisms causing GW emission during the postmerger evolution. However, we want to understand if the presence of a SQM core changes the standard picture of the characteristic postmerger spectrum estimated for hadronic matter, see also [17,18].

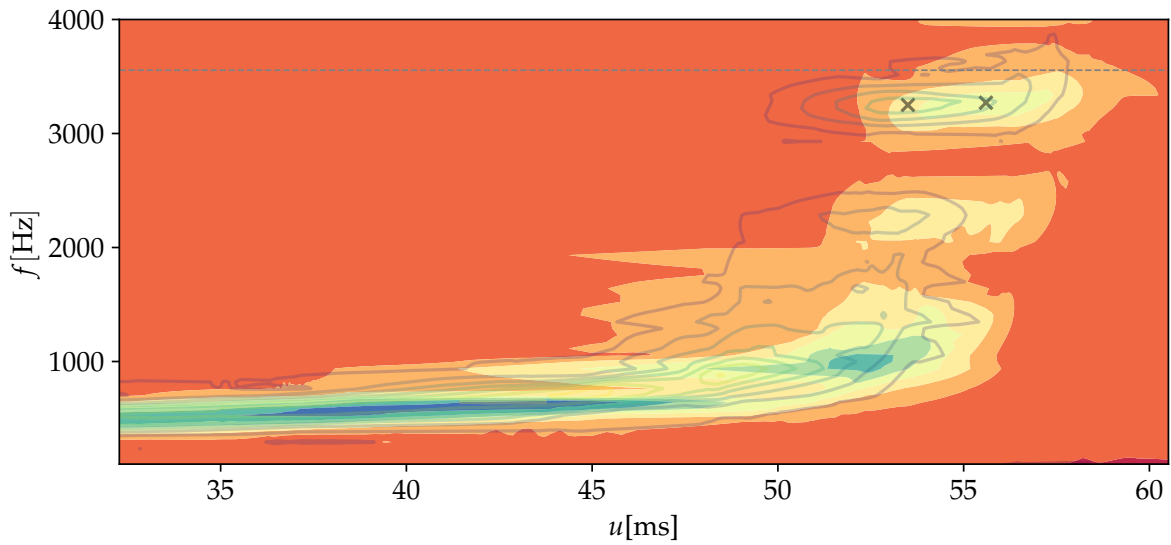


**Figure 6.** Spectrogram for resolution R4 (filled contours) and resolution R3 (solid lines). We mark the dominant postmerger frequency for the two resolutions as black crosses. In addition we include as a horizontal dashed line the postmerger frequency estimate derived from Ref. [83].

For a better understanding of the frequency evolution, we present the spectrogram of the dominant (2,2)-mode of the GW signal in Fig. 6; we refer to Ref. [84] for a detailed discussion about the computation of the spectrogram. For our setup, the merger remnant collapses within  $\sim 5$  ms to a BH, due to this very short time the postmerger GW emission is not very strong. Nevertheless, one can extract the main emission frequency  $f_2$  and obtains an emission of

$$f_2 = (3.27 \pm 0.1) \text{ kHz}, \quad (19)$$

where the uncertainty is determined as the difference between the two highest available resolutions and also includes the uncertainty caused by the finite width of the peak in the frequency domain spectrum. We compare this  $f_2$  frequency with the quasi-universal relation expressed in Ref. [83] derived from pure

hadronic EoSs. For a combined tidal deformability of  $\tilde{\Lambda} = 378^3$  Ref. [83] predicts  $f_2 = 3.55\text{kHz}$ . We visualize this estimate as a horizontal dotted line in Fig. 6.

Overall, the difference of 0.3kHz between our measurement and the quasi-universal relation is consistent with the uncertainty of the phenomenological fit [83] combined with the uncertainty of our NR data. Thus, no clear imprint of the SQM core of the merger remnant on the postmerger evolution is present. This is opposite to the work of [18] in which the merger remnant undergoes a first order phase transition which changes significantly the postmerger spectrum leading to a main emission frequency about 450 *rmHz* higher than the one predicted for a pure hadronic EoS. However, since the SQM imprint on the postmerger dynamics will depend on the exact EoS, our results are not in contradiction or tension to [18]. Similar to our results Ref. [17] finds a shorter merger remnant lifetime in the presence of a phase transition, but a similar postmerger frequency evolution as for pure hadronic matter.

## 6. Ejecta and electromagnetic counterparts

In addition to the emission of GWs, NS mergers are associated with a variety of EM signals such as short gamma-ray bursts (GRB), a synchrotron afterglow, and a thermal kilonova.

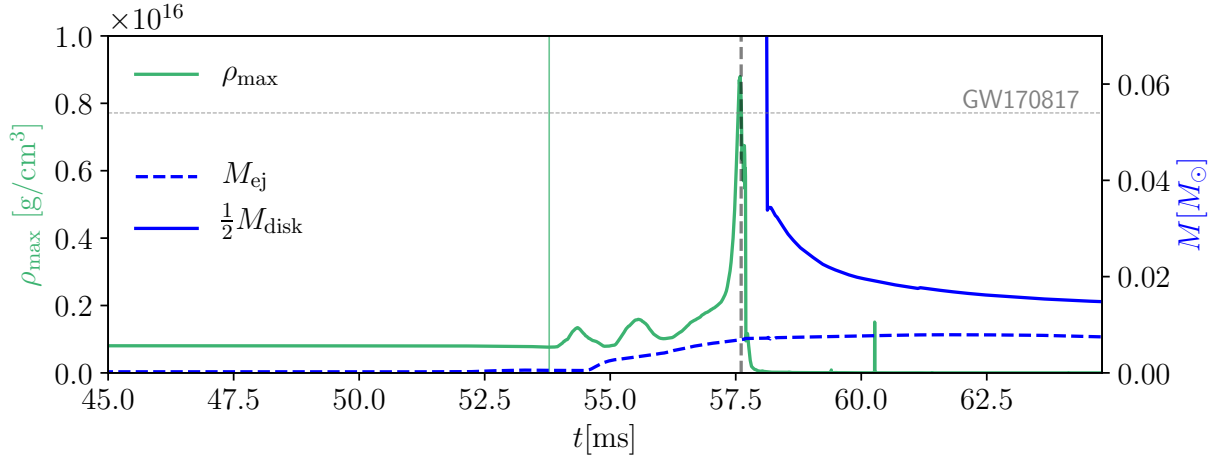


**Figure 7.** Time evolution of the maximum density (green) and the amount of ejected material (dashed blue) and the disk mass (solid blue) for resolution R3. The ejected material is estimated according to Eqs. (14) and (15) of [52], i.e., all material is marked as ejecta as long as it is gravitationally unbound and has an outward pointing velocity.

The thermal kilonova originates from neutron-rich outflows and the radioactive decay of *r*-process elements in the ejected matter, see e.g. [85] and references therein. Kilonovae produce an almost isotropic EM emission and are visible in the ultraviolet/optical/infrared band. Current analyses of the kilonova AT2017gfo associated with GW170817 estimate the ejecta mass to be  $\sim 5 \times 10^{-2} M_{\odot}$ . In our work, we will assume  $\sim 5.4 \times 10^{-2} M_{\odot}$  as found in [13].

We present the amount of ejected matter present over the course of our simulation in Fig. 7 as a blue dashed line. We find that after the merger, the maximum density of the NS remnant increases and 3 oscillations are found. During this time most of the ejection happens and at the end of our simulation the ejecta mass is about  $\sim 0.8 \times 10^{-2} M_{\odot}$ . This estimate agrees to about 30% with resolution R3, which shows the overall consistency of our dataset. For comparison, the ejecta mass obtained in equal-mass

<sup>3</sup> The combined tidal deformability  $\tilde{\Lambda}$  equals the individual tidal deformabilities  $\Lambda^{A,B}$  presented in Tab. 1 for equal-mass binary stars.

BNS simulations employing SLy EoS with similar grid configurations and masses (Tab. III of Ref. [70], with  $M^{A,B} = 1.37M_{\odot}$  and Tab. V of Ref. [52], with  $M^{A,B} = 1.35M_{\odot}$ ) are, respectively,  $1.6 \times 10^{-2}M_{\odot}$  and  $1.22 \times 10^{-2}M_{\odot}$ . Consequently, our binary HyS configuration ejects only half of the amount of dynamical ejecta mass when compared to simulations employing the purely hadronic EOS SLy [52,70]<sup>4</sup>.

Due to the short evolution time after the merger, we are unable to estimate the total amount of ejecta due to the missing disk wind driven outflows which happen on longer timescales, see e.g. [87–97]. However, we find that the disk mass drops to about  $\sim 3.4 \times 10^{-2}M_{\odot}$  towards the end of our simulation. Compared to the SLy simulations in Refs. [52,70] this is only about  $\sim 15$  to 40% of the SLy simulations. This means that if even half of the disk would be ejected (see Fig. 7), the kilonova associated with our studied HyS configuration would not be as bright as it was observed for GW170817.

Overall, the comparison of the ejecta and disk mass of our binary HyS and an SLy BNS suggests that HyS systems retain more mass within the stars along the time evolution and create dimmer EM counterparts. Further studies are necessary in order to understand whether this behavior is universal or restricted to our SQM EoS parameters choice.

To estimate the absolute magnitude of the kilonova connected to the HyS merger, we use the kilonova model of [11,98]. The model of [98] employs a multi-dimensional Monte Carlo code to solve the multi-wavelength radiation transport equation for a relativistically expanding medium. To obtain the final predicted lightcurves, we interpolate between the existing Monte Carlo simulations using the Gaussian Process Regression techniques discussed in [11]. For our estimates, we use the dynamical ejecta component  $M_{\text{ej,dyn}} = 8 \times 10^{-3}M_{\odot}$  which leaves the system with an average velocity of  $v_{\text{ej,dyn}} = 0.2$ . Furthermore, we assume a lanthanide fraction  $X_{\text{ej,dyn}} = 10^{-1}$ . For the disk wind ejecta, we assume a velocity of  $v_{\text{ej,wind}} = 0.1c$ , a lanthanide fraction of  $10^{-4}$ , and an ejecta mass of  $M_{\text{ej,wind}} = 0.017M_{\odot}$ . The largest absolute magnitudes are obtained in the near-infrared, e.g. i- and K-band, while in the optical and ultraviolet the signal is fainter, see Fig. 8.

In contrast to the kilonova, short GRBs are created by highly relativistic outflows, powered by the merger remnant accretion disk, e.g., [99,100]. Based on the measured accretion disk mass of  $\sim 3 \times 10^{-2}M_{\odot}$  at the end of our simulation, we can obtain an order of magnitude estimate for the energy which could be released by a potential short GRB. Assuming that the GRB energy is proportional to the disk mass and that the proportionality constant is of about  $10^{-2}$  as estimated in [13], we find a GRB energy of  $3 \sim 10^{-4}M_{\odot}$ , i.e.,  $6 \times 10^{50}$  erg, which is consistent with current observational constraints for GRB170817A, e.g., [101].

## 7. Conclusion

In this work, we presented and discussed the general procedure to construct HyS EoSs combining the tdBag model for SQM and a HM EoS for low-density material. Our procedure can be applied to study a variety of parameters and HM EoS choice and enables future studies of NSs binary containing SQM cores. The GW signal obtained from our NR simulations of a non-spinning, equal mass binary HyS merger exhibits a larger dephasing caused by numerical discretization than similar simulations for purely hadronic BNS configurations. We point out that the presence of a strong phase transition inside the stars can lead to a drop of the convergence to 1st order for insufficient resolutions even though higher order

---

<sup>4</sup> We note that the phenomenological fit for hadronic EOSs for the dynamical ejecta mass proposed in [13] (which is an updated version of the work presented in [86]) predicts a dynamical ejecta mass of  $0.28 \times 10^{-2}M_{\odot}$ , which lies even below our results. The discrepancy between the fit and the SLy simulations is caused by the large shock driven ejecta for the SLy EOS, which seems not to be fully captured in [13]. In addition, this comparison shows that further work with a larger set of HyS EOSs is required to obtain further confidence in the ejecta properties of NR simulations.

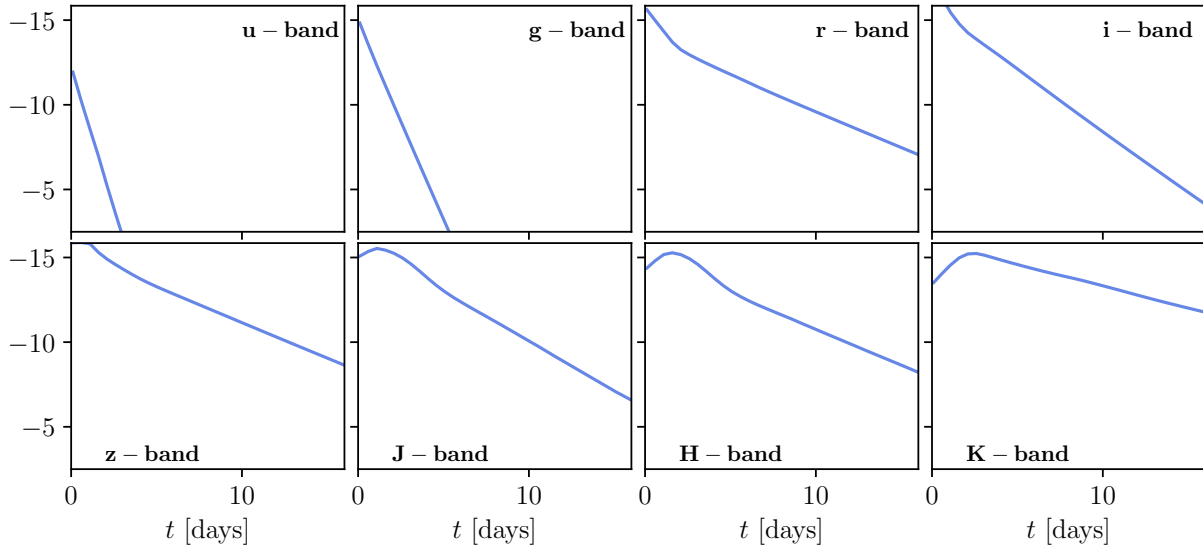


**Figure 8.** Estimated absolute magnitude of the kilonova in different frequency band using the methods outlined in [11,98].

methods are applied. This is evidence that HyS mergers add additional complexity to the NR simulations. Further simulations must be done in order to understand if these features are universal or caused by the particular choice of EoS in connection with the employed numerical methods. Furthermore, we show that the postmerger GW main emission frequency for our constructed EoS is consistent with quasi-universal relations derived from hadronic EoSs within the uncertainties of the relation. Performing an analysis of the ejecta properties and EM signatures, the kilonova and the short GRB, we are able to draw the full multi-messenger picture for our HyS merger simulation. Our work is the first step towards a better coverage of the BNS parameter space and enables future investigations of a wider range of EoS with full NR simulations.

1. Abbott, B.P.; others. GW170817: Observation of Gravitational Waves from a Binary Neutron Star Inspiral. *Phys. Rev. Lett.* **2017**, *119*, 161101, [arXiv:gr-qc/1710.05832]. doi:10.1103/PhysRevLett.119.161101.
2. Abbott, B.P.; others. Multi-messenger Observations of a Binary Neutron Star Merger. *Astrophys. J.* **2017**, *848*, L12, [arXiv:astro-ph.HE/1710.05833]. doi:10.3847/2041-8213/aa91c9.
3. Abbott, B.P.; others. Gravitational Waves and Gamma-rays from a Binary Neutron Star Merger: GW170817 and GRB 170817A. *Astrophys. J.* **2017**, *848*, L13, [arXiv:astro-ph.HE/1710.05834]. doi:10.3847/2041-8213/aa920c.
4. Dai, L.; Venumadhav, T.; Zackay, B. Parameter Estimation for GW170817 using Relative Binning **2018**. [arXiv:gr-qc/1806.08793].
5. De, S.; Finstad, D.; Lattimer, J.M.; Brown, D.A.; Berger, E.; Biwer, C.M. Tidal Deformabilities and Radii of Neutron Stars from the Observation of GW170817. *Phys. Rev. Lett.* **2018**, *121*, 091102, [arXiv:astro-ph.HE/1804.08583]. [Erratum: *Phys. Rev. Lett.*121,no.25,259902(2018)], doi:10.1103/PhysRevLett.121.259902, 10.1103/PhysRevLett.121.091102.
6. Abbott, B.P.; others. Properties of the binary neutron star merger GW170817. *Phys. Rev.* **2019**, *X9*, 011001, [arXiv:gr-qc/1805.11579]. doi:10.1103/PhysRevX.9.011001.
7. Abbott, B.P.; others. GW170817: Measurements of neutron star radii and equation of state. *Phys. Rev. Lett.* **2018**, *121*, 161101, [arXiv:gr-qc/1805.11581]. doi:10.1103/PhysRevLett.121.161101.

8. Abbott, B.P.; others. GWTC-1: A Gravitational-Wave Transient Catalog of Compact Binary Mergers Observed by LIGO and Virgo during the First and Second Observing Runs **2018**. [arXiv:astro-ph.HE/1811.12907].
9. Radice, D.; Perego, A.; Zappa, F.; Bernuzzi, S. GW170817: Joint Constraint on the Neutron Star Equation of State from Multimessenger Observations. *Astrophys. J.* **2018**, *852*, L29, [arXiv:astro-ph.HE/1711.03647]. doi:10.3847/2041-8213/aaa402.
10. Bauswein, A.; Just, O.; Janka, H.T.; Stergioulas, N. Neutron-star radius constraints from GW170817 and future detections. *Astrophys. J.* **2017**, *850*, L34, [arXiv:astro-ph.HE/1710.06843]. doi:10.3847/2041-8213/aa9994.
11. Coughlin, M.W.; others. Constraints on the neutron star equation of state from AT2017gfo using radiative transfer simulations **2018**. [arXiv:astro-ph.HE/1805.09371]. doi:10.1093/mnras/sty2174.
12. Radice, D.; Dai, L. Multimessenger Parameter Estimation of GW170817 **2018**. [arXiv:astro-ph.HE/1810.12917].
13. Coughlin, M.W.; Dietrich, T.; Margalit, B.; Metzger, B.D. Multi-messenger Bayesian parameter inference of a binary neutron-star merger **2018**. [arXiv:astro-ph.HE/1812.04803].
14. Annala, E.; Gorda, T.; Kurkela, A.; Vuorinen, A. Gravitational-wave constraints on the neutron-star-matter Equation of State. *Phys. Rev. Lett.* **2018**, *120*, 172703, [arXiv:astro-ph.HE/1711.02644]. doi:10.1103/PhysRevLett.120.172703.
15. Most, E.R.; Weih, L.R.; Rezzolla, L.; Schaffner-Bielich, J. New constraints on radii and tidal deformabilities of neutron stars from GW170817. *Phys. Rev. Lett.* **2018**, *120*, 261103, [arXiv:gr-qc/1803.00549]. doi:10.1103/PhysRevLett.120.261103.
16. Annala, E.; Gorda, T.; Kurkela, A.; Nättilä, J.; Vuorinen, A. Quark-matter cores in neutron stars **2019**. [arXiv:astro-ph.HE/1903.09121].
17. Most, E.R.; Papenfort, L.J.; Dexheimer, V.; Hanauske, M.; Schramm, S.; Stöcker, H.; Rezzolla, L. Signatures of quark-hadron phase transitions in general-relativistic neutron-star mergers. *Phys. Rev. Lett.* **2019**, *122*, 061101, [arXiv:astro-ph.HE/1807.03684]. doi:10.1103/PhysRevLett.122.061101.
18. Bauswein, A.; Bastian, N.U.F.; Blaschke, D.B.; Chatziioannou, K.; Clark, J.A.; Fischer, T.; Oertel, M. Identifying a first-order phase transition in neutron star mergers through gravitational waves. *Phys. Rev. Lett.* **2019**, *122*, 061102, [arXiv:astro-ph.HE/1809.01116]. doi:10.1103/PhysRevLett.122.061102.
19. Radice, D.; Rezzolla, L.; Galeazzi, F. Beyond second-order convergence in simulations of binary neutron stars in full general-relativity. *Mon. Not. Roy. Astron. Soc.* **2014**, *437*, L46–L50, [arXiv:gr-qc/1306.6052]. doi:10.1093/mnrasl/slt137.
20. Hotokezaka, K.; Kyutoku, K.; Okawa, H.; Shibata, M. Exploring tidal effects of coalescing binary neutron stars in numerical relativity. II. Long-term simulations. *Phys. Rev.* **2015**, *D91*, 064060, [arXiv:gr-qc/1502.03457]. doi:10.1103/PhysRevD.91.064060.
21. Dietrich, T.; Bernuzzi, S.; Tichy, W. Closed-form tidal approximants for binary neutron star gravitational waveforms constructed from high-resolution numerical relativity simulations. *Phys. Rev.* **2017**, *D96*, 121501, [arXiv:gr-qc/1706.02969]. doi:10.1103/PhysRevD.96.121501.
22. Kiuchi, K.; Kawaguchi, K.; Kyutoku, K.; Sekiguchi, Y.; Shibata, M.; Taniguchi, K. Sub-radian-accuracy gravitational waveforms of coalescing binary neutron stars in numerical relativity. *Phys. Rev.* **2017**, *D96*, 084060, [arXiv:astro-ph.HE/1708.08926]. doi:10.1103/PhysRevD.96.084060.
23. Dietrich, T.; Radice, D.; Bernuzzi, S.; Zappa, F.; Perego, A.; Brüggmann, B.; Chaurasia, S.V.; Dudi, R.; Tichy, W.; Ujevic, M. CoRe database of binary neutron star merger waveforms. *Class. Quant. Grav.* **2018**, *35*, 24LT01, [arXiv:gr-qc/1806.01625]. doi:10.1088/1361-6382/aaebc0.
24. Rezzolla, L.; Giacomazzo, B.; Baiotti, L.; Granot, J.; Kouveliotou, C.; Aloy, M.A. The missing link: Merging neutron stars naturally produce jet-like structures and can power short Gamma-Ray Bursts. *Astrophys. J.* **2011**, *732*, L6, [arXiv:astro-ph.HE/1101.4298]. doi:10.1088/2041-8205/732/1/L6.
25. Neilsen, D.; Liebling, S.L.; Anderson, M.; Lehner, L.; O'Connor, E.; Palenzuela, C. Magnetized Neutron Stars With Realistic Equations of State and Neutrino Cooling. *Phys. Rev.* **2014**, *D89*, 104029, [arXiv:gr-qc/1403.3680]. doi:10.1103/PhysRevD.89.104029.



26. Sekiguchi, Y.; Kiuchi, K.; Kyutoku, K.; Shibata, M. Dynamical mass ejection from binary neutron star mergers: Radiation-hydrodynamics study in general relativity. *Phys. Rev.* **2015**, *D91*, 064059, [arXiv:astro-ph.HE/1502.06660]. doi:10.1103/PhysRevD.91.064059.
27. Palenzuela, C.; Liebling, S.L.; Neilsen, D.; Lehner, L.; Caballero, O.L.; O'Connor, E.; Anderson, M. Effects of the microphysical Equation of State in the mergers of magnetized Neutron Stars With Neutrino Cooling. *Phys. Rev.* **2015**, *D92*, 044045, [arXiv:gr-qc/1505.01607]. doi:10.1103/PhysRevD.92.044045.
28. Foucart, F. Monte Carlo closure for moment-based transport schemes in general relativistic radiation hydrodynamic simulations. *Mon. Not. Roy. Astron. Soc.* **2018**, *475*, 4186–4207, [arXiv:astro-ph.HE/1708.08452]. doi:10.1093/mnras/sty108.
29. Ruiz, M.; Shapiro, S.L.; Tsokaros, A. GW170817, General Relativistic Magnetohydrodynamic Simulations, and the Neutron Star Maximum Mass. *Phys. Rev.* **2018**, *D97*, 021501, [arXiv:astro-ph.HE/1711.00473]. doi:10.1103/PhysRevD.97.021501.
30. Cioffi, R.; Kastaun, W.; Giacomazzo, B.; Endrizzi, A.; Siegel, D.M.; Perna, R. General relativistic magnetohydrodynamic simulations of binary neutron star mergers forming a long-lived neutron star. *Phys. Rev.* **2017**, *D95*, 063016, [arXiv:astro-ph.HE/1701.08738]. doi:10.1103/PhysRevD.95.063016.
31. Kiuchi, K.; Kyutoku, K.; Sekiguchi, Y.; Shibata, M. Global simulations of strongly magnetized remnant massive neutron stars formed in binary neutron star mergers. *Phys. Rev.* **2018**, *D97*, 124039, [arXiv:astro-ph.HE/1710.01311]. doi:10.1103/PhysRevD.97.124039.
32. Radice, D. General-Relativistic Large-Eddy Simulations of Binary Neutron Star Mergers. *Astrophys. J.* **2017**, *838*, L2, [arXiv:astro-ph.HE/1703.02046]. doi:10.3847/2041-8213/aa6483.
33. Shibata, M.; Kiuchi, K.; Sekiguchi, Y. General relativistic viscous hydrodynamics of differentially rotating neutron stars. *Phys. Rev.* **2017**, *D95*, 083005, [arXiv:astro-ph.HE/1703.10303]. doi:10.1103/PhysRevD.95.083005.
34. Pietri, R.d.; Drago, A.; Feo, A.; Pagliara, G.; Pasquali, M.; Traversi, S.; Wiktorowicz, G. Merger of Compact Stars in the Two-Families Scenario **2019**. [arXiv:astro-ph.HE/1904.01545].
35. Farhi, E.; Jaffe, R.L. Strange Matter. *Phys. Rev.* **1984**, *D30*, 2379. doi:10.1103/PhysRevD.30.2379.
36. Chodos, A.; Jaffe, R.L.; Johnson, K.; Thorn, C.B.; Weisskopf, V.F. A New Extended Model of Hadrons. *Phys. Rev.* **1974**, *D9*, 3471–3495. doi:10.1103/PhysRevD.9.3471.
37. Detar, C.E. THE MIT BAG MODEL. NATO Advanced Study Institute in Elementary Particles: Quantum Flavordynamics, Quantum Chromodynamics and Unified Theories Boulder, Colo., July 9-27, 1979, 1979, p. 393.
38. Alford, M.; Braby, M.; Paris, M.W.; Reddy, S. Hybrid stars that masquerade as neutron stars. *Astrophys. J.* **2005**, *629*, 969–978, [arXiv:nucl-th/nucl-th/0411016]. doi:10.1086/430902.
39. Alford, M.G.; Schmitt, A.; Rajagopal, K.; Schäfer, T. Color superconductivity in dense quark matter. *Rev. Mod. Phys.* **2008**, *80*, 1455–1515, [arXiv:hep-ph/0709.4635]. doi:10.1103/RevModPhys.80.1455.
40. Lugones, G.; Horvath, J.E. Color flavor locked strange matter. *Phys. Rev.* **2002**, *D66*, 074017, [arXiv:hep-ph/hep-ph/0211070]. doi:10.1103/PhysRevD.66.074017.
41. Fraga, E.S.; Pisarski, R.D.; Schaffner-Bielich, J. Small, dense quark stars from perturbative QCD. *Phys. Rev.* **2001**, *D63*, 121702, [arXiv:hep-ph/hep-ph/0101143]. doi:10.1103/PhysRevD.63.121702.
42. Klahn, T.; Fischer, T. Vector interaction enhanced bag model for astrophysical applications. *Astrophys. J.* **2015**, *810*, 134, [arXiv:nucl-th/1503.07442]. doi:10.1088/0004-637X/810/2/134.
43. Pereira, J.P.; Flores, C.V.; Lugones, G. Phase transition effects on the dynamical stability of hybrid neutron stars. *Astrophys. J.* **2018**, *860*, 12, [arXiv:gr-qc/1706.09371]. doi:10.3847/1538-4357/aabfbf.
44. Bodmer, A.R. Collapsed nuclei. *Phys. Rev.* **1971**, *D4*, 1601–1606. doi:10.1103/PhysRevD.4.1601.
45. Witten, E. Cosmic Separation of Phases. *Phys. Rev.* **1984**, *D30*, 272–285. doi:10.1103/PhysRevD.30.272.
46. Glendenning, N.K. *Compact Stars: Nuclear Physics, Particle Physics, and General Relativity*, 2 ed.; Springer: The address, 2000.
47. Lugones, G.; Grunfeld, A.G.; Al Ajmi, M. Surface tension and curvature energy of quark matter in the Nambu-Jona-Lasinio model. *Phys. Rev.* **2013**, *C88*, 045803, [arXiv:hep-ph/1308.1452]. doi:10.1103/PhysRevC.88.045803.

48. Nambu, Y.; Jona-Lasinio, G. Dynamical Model of Elementary Particles Based on an Analogy with Superconductivity. 1. *Phys. Rev.* **1961**, *122*, 345–358. [127(1961)], doi:10.1103/PhysRev.122.345.
49. Douchin, F.; Haensel, P. A unified equation of state of dense matter and neutron star structure. *Astron. Astrophys.* **2001**, *380*, 151, [arXiv:astro-ph/astro-ph/0111092]. doi:10.1051/0004-6361:20011402.
50. Bruegmann, B.; Gonzalez, J.A.; Hannam, M.; Husa, S.; Sperhake, U.; Tichy, W. Calibration of Moving Puncture Simulations. *Phys. Rev.* **2008**, *D77*, 024027, [arXiv:gr-qc/gr-qc/0610128]. doi:10.1103/PhysRevD.77.024027.
51. Thierfelder, M.; Bernuzzi, S.; Bruegmann, B. Numerical relativity simulations of binary neutron stars. *Phys. Rev.* **2011**, *D84*, 044012, [arXiv:gr-qc/1104.4751]. doi:10.1103/PhysRevD.84.044012.
52. Dietrich, T.; Bernuzzi, S.; Ujevic, M.; Brüggmann, B. Numerical relativity simulations of neutron star merger remnants using conservative mesh refinement. *Phys. Rev.* **2015**, *D91*, 124041, [arXiv:gr-qc/1504.01266]. doi:10.1103/PhysRevD.91.124041.
53. Bernuzzi, S.; Dietrich, T. Gravitational waveforms from binary neutron star mergers with high-order weighted-essentially-nonscillatory schemes in numerical relativity. *Phys. Rev.* **2016**, *D94*, 064062, [arXiv:gr-qc/1604.07999]. doi:10.1103/PhysRevD.94.064062.
54. Tichy, W. A New numerical method to construct binary neutron star initial data. *Class. Quant. Grav.* **2009**, *26*, 175018, [arXiv:gr-qc/0908.0620]. doi:10.1088/0264-9381/26/17/175018.
55. Read, J.S.; Lackey, B.D.; Owen, B.J.; Friedman, J.L. Constraints on a phenomenologically parameterized neutron-star equation of state. *Phys. Rev.* **2009**, *D79*, 124032, [arXiv:astro-ph/0812.2163]. doi:10.1103/PhysRevD.79.124032.
56. Wilson, J.R.; Mathews, G.J. Instabilities in Close Neutron Star Binaries. *Phys. Rev. Lett.* **1995**, *75*, 4161–4164. doi:10.1103/PhysRevLett.75.4161.
57. Wilson, J.R.; Mathews, G.J.; Marronetti, P. Relativistic numerical model for close neutron star binaries. *Phys. Rev.* **1996**, *D54*, 1317–1331, [arXiv:gr-qc/gr-qc/9601017]. doi:10.1103/PhysRevD.54.1317.
58. York, Jr., J.W. Conformal ‘thin sandwich’ data for the initial-value problem. *Phys. Rev. Lett.* **1999**, *82*, 1350–1353, [arXiv:gr-qc/gr-qc/9810051]. doi:10.1103/PhysRevLett.82.1350.
59. Tichy, W. Constructing quasi-equilibrium initial data for binary neutron stars with arbitrary spins. *Phys. Rev. D* **2012**, *86*, 064024, [arXiv:gr-qc/1209.5336]. doi:10.1103/PhysRevD.86.064024.
60. Dietrich, T.; Moldenhauer, N.; Johnson-McDaniel, N.K.; Bernuzzi, S.; Markakis, C.M.; Brüggmann, B.; Tichy, W. Binary Neutron Stars with Generic Spin, Eccentricity, Mass ratio, and Compactness - Quasi-equilibrium Sequences and First Evolutions. *Phys. Rev.* **2015**, *D92*, 124007, [arXiv:gr-qc/1507.07100]. doi:10.1103/PhysRevD.92.124007.
61. Moldenhauer, N.; Markakis, C.M.; Johnson-McDaniel, N.K.; Tichy, W.; Brüggmann, B. Initial data for binary neutron stars with adjustable eccentricity. *Phys. Rev.* **2014**, *D90*, 084043, [arXiv:gr-qc/1408.4136]. doi:10.1103/PhysRevD.90.084043.
62. Kyutoku, K.; Shibata, M.; Taniguchi, K. Reducing orbital eccentricity in initial data of binary neutron stars. *Phys. Rev.* **2014**, *D90*, 064006, [arXiv:gr-qc/1405.6207]. doi:10.1103/PhysRevD.90.064006.
63. Bernuzzi, S.; Hilditch, D. Constraint violation in free evolution schemes: Comparing BSSNOK with a conformal decomposition of Z4. *Phys. Rev.* **2010**, *D81*, 084003, [arXiv:gr-qc/0912.2920]. doi:10.1103/PhysRevD.81.084003.
64. Weyhausen, A.; Bernuzzi, S.; Hilditch, D. Constraint damping for the Z4c formulation of general relativity. *Phys. Rev.* **2012**, *D85*, 024038, [arXiv:gr-qc/1107.5539]. doi:10.1103/PhysRevD.85.024038.
65. Hilditch, D.; Bernuzzi, S.; Thierfelder, M.; Cao, Z.; Tichy, W.; Bruegmann, B. Compact binary evolutions with the Z4c formulation. *Phys. Rev.* **2013**, *D88*, 084057, [arXiv:gr-qc/1212.2901]. doi:10.1103/PhysRevD.88.084057.
66. Borges, R.; Carmona, M.; Costa, B.; Don, W.S. An improved weighted essentially non-oscillatory scheme for hyperbolic conservation laws. *Journal of Computational Physics* **2008**, *227*, 3191–3211. doi:10.1016/j.jcp.2007.11.038.
67. Dietrich, T.; Bernuzzi, S.; Bruegmann, B.; Tichy, W. High-resolution numerical relativity simulations of spinning binary neutron star mergers. Proceedings, 26th Euromicro International Conference on Parallel, Distributed and Network-based Processing (PDP 2018): Cambridge, UK, March 21-23, 2018, 2018, pp. 682–689, [arXiv:gr-qc/1803.07965]. doi:10.1109/PDP2018.2018.00113.

68. Faber, J.A.; Rasio, F.A. Binary Neutron Star Mergers. *Living Rev.Rel.* **2012**, *15*, 8, [arXiv:gr-qc/1204.3858].
69. Dietrich, T.; others. Matter imprints in waveform models for neutron star binaries: Tidal and self-spin effects. *Phys. Rev.* **2019**, *D99*, 024029, [arXiv:gr-qc/1804.02235]. doi:10.1103/PhysRevD.99.024029.
70. Dietrich, T.; Ujevic, M.; Tichy, W.; Bernuzzi, S.; Bruegmann, B. Gravitational waves and mass ejecta from binary neutron star mergers: Effect of the mass-ratio. *Phys. Rev.* **2017**, *D95*, 024029, [arXiv:gr-qc/1607.06636]. doi:10.1103/PhysRevD.95.024029.
71. Dietrich, T.; Bernuzzi, S.; Ujevic, M.; Tichy, W. Gravitational waves and mass ejecta from binary neutron star mergers: Effect of the stars' rotation. *Phys. Rev.* **2017**, *D95*, 044045, [arXiv:gr-qc/1611.07367]. doi:10.1103/PhysRevD.95.044045.
72. Hannam, M.; Schmidt, P.; Bohé, A.; Haegel, L.; Husa, S.; Ohme, F.; Pratten, G.; Pürrer, M. Simple Model of Complete Precessing Black-Hole-Binary Gravitational Waveforms. *Phys. Rev. Lett.* **2014**, *113*, 151101, [arXiv:gr-qc/1308.3271]. doi:10.1103/PhysRevLett.113.151101.
73. Abbott, B.P.; others. Tests of General Relativity with GW170817 **2018**. [arXiv:gr-qc/1811.00364].
74. Takami, K.; Rezzolla, L.; Baiotti, L. Constraining the Equation of State of Neutron Stars from Binary Mergers. *Phys. Rev. Lett.* **2014**, *113*, 091104, [arXiv:gr-qc/1403.5672]. doi:10.1103/PhysRevLett.113.091104.
75. Takami, K.; Rezzolla, L.; Baiotti, L. Spectral properties of the post-merger gravitational-wave signal from binary neutron stars. *Phys. Rev.* **2015**, *D91*, 064001, [arXiv:gr-qc/1412.3240]. doi:10.1103/PhysRevD.91.064001.
76. Rezzolla, L.; Takami, K. Gravitational-wave signal from binary neutron stars: a systematic analysis of the spectral properties. *Phys. Rev.* **2016**, *D93*, 124051, [arXiv:gr-qc/1604.00246]. doi:10.1103/PhysRevD.93.124051.
77. Bauswein, A.; Janka, H.T. Measuring neutron-star properties via gravitational waves from binary mergers. *Phys. Rev. Lett.* **2012**, *108*, 011101, [arXiv:astro-ph.SR/1106.1616]. doi:10.1103/PhysRevLett.108.011101.
78. Stergioulas, N.; Bauswein, A.; Zagkouris, K.; Janka, H.T. Gravitational waves and nonaxisymmetric oscillation modes in mergers of compact object binaries. *Mon. Not. Roy. Astron. Soc.* **2011**, *418*, 427, [arXiv:gr-qc/1105.0368]. doi:10.1111/j.1365-2966.2011.19493.x.
79. Bauswein, A.; Janka, H.T.; Hebeler, K.; Schwenk, A. Equation-of-state dependence of the gravitational-wave signal from the ring-down phase of neutron-star mergers. *Phys. Rev.* **2012**, *D86*, 063001, [arXiv:astro-ph.SR/1204.1888]. doi:10.1103/PhysRevD.86.063001.
80. Bauswein, A.; Stergioulas, N.; Janka, H.T. Revealing the high-density equation of state through binary neutron star mergers. *Phys. Rev.* **2014**, *D90*, 023002, [arXiv:astro-ph.SR/1403.5301]. doi:10.1103/PhysRevD.90.023002.
81. Clark, J.A.; Bauswein, A.; Stergioulas, N.; Shoemaker, D. Observing Gravitational Waves From The Post-Merger Phase Of Binary Neutron Star Coalescence. *Class. Quant. Grav.* **2016**, *33*, 085003, [arXiv:astro-ph.HE/1509.08522]. doi:10.1088/0264-9381/33/8/085003.
82. Bauswein, A.; Stergioulas, N. Unified picture of the post-merger dynamics and gravitational wave emission in neutron star mergers. *Phys. Rev.* **2015**, *D91*, 124056, [arXiv:astro-ph.SR/1502.03176]. doi:10.1103/PhysRevD.91.124056.
83. Bernuzzi, S.; Dietrich, T.; Nagar, A. Modeling the complete gravitational wave spectrum of neutron star mergers. *Phys. Rev. Lett.* **2015**, *115*, 091101, [arXiv:gr-qc/1504.01764]. doi:10.1103/PhysRevLett.115.091101.
84. Chaurasia, S.V.; Dietrich, T.; Johnson-McDaniel, N.K.; Ujevic, M.; Tichy, W.; Brüggmann, B. Gravitational waves and mass ejecta from binary neutron star mergers: Effect of large eccentricities. *Phys. Rev.* **2018**, *D98*, 104005, [arXiv:gr-qc/1807.06857]. doi:10.1103/PhysRevD.98.104005.
85. Metzger, B.D. Kilonovae. *Living Rev. Rel.* **2017**, *20*, 3, [arXiv:astro-ph.HE/1610.09381]. doi:10.1007/s41114-017-0006-z.
86. Dietrich, T.; Ujevic, M. Modeling dynamical ejecta from binary neutron star mergers and implications for electromagnetic counterparts. *Class. Quant. Grav.* **2017**, *34*, 105014, [arXiv:gr-qc/1612.03665]. doi:10.1088/1361-6382/aa6bb0.
87. Kohri, K.; Narayan, R.; Piran, T. Neutrino-dominated accretion and supernovae. *Astrophys. J.* **2005**, *629*, 341–361, [arXiv:astro-ph/astro-ph/0502470]. doi:10.1086/431354.
88. Surman, R.; McLaughlin, G.C.; Hix, W.R. Nucleosynthesis in the outflow from gamma-ray burst accretion disks. *Astrophys. J.* **2006**, *643*, 1057–1064, [arXiv:astro-ph/astro-ph/0509365]. doi:10.1086/501116.

89. Metzger, B.D.; Piro, A.L.; Quataert, E. Time-Dependent Models of Accretion Disks Formed from Compact Object Mergers. *Mon. Not. Roy. Astron. Soc.* **2008**, *390*, 781, [arXiv:astro-ph/0805.4415]. doi:10.1111/j.1365-2966.2008.13789.x.
90. Dessart, L.; Ott, C.D.; Burrows, A.; Rosswog, S.; Livne, E. Neutrino signatures and the neutrino-driven wind in Binary Neutron Star Mergers. *Astrophys. J.* **2009**, *690*, 1681, [arXiv:astro-ph/0806.4380]. doi:10.1088/0004-637X/690/2/1681.
91. Fernández, R.; Metzger, B.D. Delayed outflows from black hole accretion tori following neutron star binary coalescence. *Mon. Not. Roy. Astron. Soc.* **2013**, *435*, 502, [arXiv:astro-ph.HE/1304.6720]. doi:10.1093/mnras/stt1312.
92. Perego, A.; Rosswog, S.; Cabezón, R.M.; Korobkin, O.; Käppeli, R.; Arcones, A.; Liebendörfer, M. Neutrino-driven winds from neutron star merger remnants. *Mon. Not. Roy. Astron. Soc.* **2014**, *443*, 3134–3156, [arXiv:astro-ph.HE/1405.6730]. doi:10.1093/mnras/stu1352.
93. Siegel, D.M.; Ciolfi, R.; Rezzolla, L. Magnetically driven winds from differentially rotating neutron stars and X-ray afterglows of short gamma-ray bursts. *Astrophys. J.* **2014**, *785*, L6, [arXiv:astro-ph.HE/1401.4544]. doi:10.1088/2041-8205/785/1/L6.
94. Just, O.; Bauswein, A.; Pulpillo, R.A.; Goriely, S.; Janka, H.T. Comprehensive nucleosynthesis analysis for ejecta of compact binary mergers. *Mon. Not. Roy. Astron. Soc.* **2015**, *448*, 541–567, [arXiv:astro-ph.SR/1406.2687]. doi:10.1093/mnras/stv009.
95. Rezzolla, L.; Kumar, P. A novel paradigm for short gamma-ray bursts with extended X-ray emission. *Astrophys. J.* **2015**, *802*, 95, [arXiv:astro-ph.HE/1410.8560]. doi:10.1088/0004-637X/802/2/95.
96. Ciolfi, R.; Siegel, D.M. Short gamma-ray bursts in the "time-reversal" scenario. *Astrophys. J.* **2015**, *798*, L36, [arXiv:astro-ph.HE/1411.2015]. doi:10.1088/2041-8205/798/2/L36.
97. Siegel, D.M.; Metzger, B.D. Three-Dimensional General-Relativistic Magnetohydrodynamic Simulations of Remnant Accretion Disks from Neutron Star Mergers: Outflows and *r*-Process Nucleosynthesis. *Phys. Rev. Lett.* **2017**, *119*, 231102, [arXiv:astro-ph.HE/1705.05473]. doi:10.1103/PhysRevLett.119.231102.
98. Kasen, D.; Metzger, B.; Barnes, J.; Quataert, E.; Ramirez-Ruiz, E. Origin of the heavy elements in binary neutron-star mergers from a gravitational wave event. *Nature* **2017**, [arXiv:astro-ph.HE/1710.05463]. [Nature551,80(2017)], doi:10.1038/nature24453.
99. Paczynski, B. Gamma-ray bursters at cosmological distances. *Astrophys. J.* **1986**, *308*, L43–L46. doi:10.1086/184740.
100. Eichler, D.; Livio, M.; Piran, T.; Schramm, D.N. Nucleosynthesis, Neutrino Bursts and Gamma-Rays from Coalescing Neutron Stars. *Nature* **1989**, *340*, 126–128. [682(1989)], doi:10.1038/340126a0.
101. van Eerten, E.T.H.; Ryan, G.; Ricci, R.; Burgess, J.M.; Wieringa, M.; Piro, L.; Cenko, S.B.; Sakamoto, T. A year in the life of GW170817: the rise and fall of a structured jet from a binary neutron star merger **2018**. [arXiv:astro-ph.HE/1808.06617].

**Author Contributions:** Conceptualization, T.D. and M.U.; methodology, T.D.; investigation, H.G., T.D., M.U.; writing—original draft preparation, H.G., T.D., M.U.; writing—review and editing, H.G., T.D., M.U.; visualization, H.G., T.D.; funding acquisition, T.D., M.U.

**Funding:** This research was funded by the European Union’s Horizon 2020 research and innovation program under grant agreement No 749145, BNSmergers. Computations were performed on the supercomputer SuperMUC at the LRZ (Munich) under the project number pr48pu. M.U. and H.G. also thanks CAPES for financial support.

**Acknowledgments:** We thank Michael Coughlin for providing us with the lightcurve data of Fig. 8. We acknowledge fruitful discussions with Sebastiano Bernuzzi, Bernd Brügmann, Wolfgang Tichy, and Tsun Ho Pang.

**Conflicts of Interest:** The authors declare no conflict of interest.

## Abbreviations

The following abbreviations are used in this manuscript:

|       |                                       |
|-------|---------------------------------------|
| BH    | Black Hole                            |
| BNS   | Binary Neutron Star                   |
| CFL   | Color-flavor-locked                   |
| EM    | Electromagnetic                       |
| EoS   | Equation of State                     |
| GRB   | Gamma Ray Burst                       |
| GRHD  | General Relativistic Hydrodynamics    |
| GW    | Gravitational Wave                    |
| HM    | Hadronic Matter                       |
| HRSC  | High-resolution Shock-capturing       |
| HyS   | Hybrid Star                           |
| LLF   | Local Lax-Friedrich                   |
| MIT   | Massachusetts Institute of Technology |
| NR    | Numerical Relativity                  |
| NS    | Neutron Star                          |
| QCD   | Quantum Chromodynamics                |
| SQM   | Strange Quark Matter                  |
| WENOZ | Weighted Essentially Non-oscillatory  |

## Appendix A HyS Piecewise Polytrope

In the following, we present the EOS parameters defining the employed HyS EOS; cf. Eq. (17) in section (2.4).

**Table A1.** Piecewise polytrope of the HyS EoS used in the simulations. The units are chosen so that the rest-mass density  $\rho$  is in  $\text{g}/\text{cm}^3$ ,  $\Gamma$  is dimensionless and  $K$  is such that the pressure  $p$  is in  $\text{g}/\text{cm}^3$ . The  $i$ -th row refers to the polytrope  $p = K_i \rho^{\Gamma_i}$ , for  $\rho_i \leq \rho \leq \rho_{i+1}$ .

| $\rho$                   | $K$                        | $\Gamma$ |
|--------------------------|----------------------------|----------|
| 0.00000                  | $3.99873 \times 10^{-8}$   | 1.357    |
| $1.46231 \times 10^{14}$ | $1.80658 \times 10^{-31}$  | 3.005    |
| $2.60400 \times 10^{14}$ | $3.76582 \times 10^{12}$   | 0.000    |
| $4.66533 \times 10^{14}$ | $1.00162 \times 10^{-167}$ | 12.242   |
| $5.06058 \times 10^{14}$ | $1.29766 \times 10^{-108}$ | 8.222    |
| $6.07892 \times 10^{14}$ | $2.18919 \times 10^{-43}$  | 3.810    |
| $7.22396 \times 10^{14}$ | $7.07726 \times 10^{-28}$  | 2.766    |
| $8.50306 \times 10^{14}$ | $7.86344 \times 10^{-21}$  | 2.294    |
| $9.92358 \times 10^{14}$ | $7.59597 \times 10^{-17}$  | 2.028    |
| $1.14929 \times 10^{15}$ | $2.58041 \times 10^{-14}$  | 1.860    |
| $1.32183 \times 10^{15}$ | $1.38093 \times 10^{-12}$  | 1.746    |
| $1.51072 \times 10^{15}$ | $2.40271 \times 10^{-11}$  | 1.664    |
| $1.71669 \times 10^{15}$ | $2.01349 \times 10^{-10}$  | 1.604    |
| $1.94048 \times 10^{15}$ | $1.02422 \times 10^{-9}$   | 1.557    |
| $2.18282 \times 10^{15}$ | $4.06158 \times 10^{-9}$   | 1.518    |